Geometrically engineered two-color time orderings in a laser-dressed atomic antenna: Shaping space-time photon correlations

Ze-an Peng,[1] Ai-xi Chen,[1,*] and Gao-xiang Li[2,†]
[1]*Department of Physics, Zhejiang Sci-Tech University, Hangzhou 310018, China*
[2]*Department of Physics, Huazhong Normal University, Wuhan 430079, China*

(Received 17 June 2022; accepted 21 November 2022; published 5 December 2022)

The space-time connection between the Mollow cascaded transitions with time orderings and the spatially directional correlated emissions of Mollow photons is analyzed theoretically in a strong laser-dressed subwavelength two-atom antenna, which supports only two-level electric dipole transitions. It can be regarded as the most prototypical collective quantum radiator to exploit the space-time quantum characteristics of the Mollow physics of resonance fluorescence. By constructing the photon filtering dynamics from the dressed two-atom antenna to a pair of quantum sensors, the frequency-resolved spatial two-point two-time correlations of different Mollow spectral lines are examined analytically in terms of the quantum sensor modes. It is shown that a rich significance of spatial directionality lies in the time orderings of cascaded emissions between different Mollow spectral lines. This feature enables the time orderings of different Mollow spectral lines to be tailored geometrically and thus prepared deterministically to produce highly directional temporal bunching effects of the Mollow photons with giant nonclassicality only for a specific two-photon detection order. The dressed two-atom system is therefore able to operate as a highly directional atomic antenna that may provide versatile applications in the fields of atom-photon-based quantum precise measurement physics and Mollow spectroscopy.

DOI: 10.1103/PhysRevA.106.063702

I. INTRODUCTION

How to control and exploit the directional scattering of radiation fields precisely and effectively has become a hotspot in the research fields of nanophotonics [1–5] and quantum optics [6–8]. Only recently has it been shown that the collective atomic systems with subwavelength geometric structures can serve as promising candidates—atomic antennas to effectively engineer directional light scattering in few-photon and multiphoton levels [9–17]. The advent of this frontier topic not only brings a new perspective to superresolution quantum imaging technology [13,15], but also stimulates the penetration of antennas, a type of electronic devices belonging to the classical category, into the quantum level [9]. In view of the fact that the well-established atom cooling and trapping techniques have paved a smooth way for the design of subwavelength atomic antennas [18–20], the present-day development of atomic antennas has ushered in a wide range of opportunities, and has been lying at the intersection of quantum optics, quantum electronics, and nanophotonics.

The directional characteristics of collective emissions displayed by atomic antennas are primarily attributed to the various forms of interference effect of different radiative modes to which the atoms radiate, such as the electromagnetic modes radiated from different atoms [17,21] and the electromagnetic polarization modes supported by different external field-induced electromagnetic multipole moments [22]. In the light of the quantum nature of atomic antennas, the research on the spatially directional collective emissions of atomic antennas is no longer constrained to the radiation intensity and scattering cross section, which are the ones most frequently concerned with in classical antenna theory, but turns to the multiphoton high-order intensity correlations that characterize the quantum characteristics of collective radiation fields [9–17]. In the in-depth exploration of two-photon and multiphoton directional collective emissions, it has been further realized that spatial interference effects can also engineer time-domain properties of collective radiative dynamics, exhibiting some novel space-time quantum effects [23–26]. Most recently, a new theoretical scheme was proposed by von Zanthier *et al.* in a simple three-atom system to skillfully tune three-photon collective spontaneous emissions by synthesizing the time-domain quantum interference of two-atom internal states and the spatial interference of three-atom collective radiation fields via a distant auxiliary atom [27]. This mechanism enables such a subwavelength three-atom system to carry applicable potentialities for superresolution quantum imaging technology.

Here we intend to take the problem of space-time quantum effects of spatially directional collective emissions one step forward by exploiting photon frequency filtering in the context of collective resonance fluorescence radiated from an atomic antenna. This consideration, to a large extent, lies in the inherent time-ordering attributes of fluorescent photons, such as the Mollow photons, which can be resolved by frequency filtering and render the strong laser-dressed quantum emitters as excellent cascaded photon sources [28–30]. However, if the nature of time orderings carried by fluorescent emissions is further endowed with spatial directionality, a new landscape of space-time quantum effects arising from spatially

*aixichen@zstu.edu.cn
†gaox@mail.ccnu.edu.cn

directional collective emissions may emerge. Obviously, atomic antennas have set up a timely and ideal stage for addressing this problem. Of particular note is that it has recently become possible to utilize frequency-resolved two-photon statistical signals to probe into quantum coherent dynamics in molecular aggregates, such as two-level dimer models, by exploiting photon frequency filtering [31]. This research progress further highlights the necessity of the application of photon frequency filtering in collective atomic systems, of course including atomic antennas, which in turn bear the potential to advance the emerging field of quantum spectroscopy [32–34].

In this paper, by constructing photon filtering mechanisms, we provide an analytic treatment to the spatial-temporal correlated quantum behaviors of spectrally resolved two-color photon statistics of collective resonance fluorescence radiated from a simple collective quantum radiator, a subwavelength-spacing two-atom system driven by a strong laser beam. The access to the obtained analytic formalism solved from photon filtering dynamics enables us to gain insight into the underlying physical mechanisms of time orderings of collective fluorescent emissions, which not only embody the internal-state transition dynamics of quantum radiator, but also depend critically on the direction of propagation of the collective radiation fields. We show that the time orderings of two Mollow spectral combinations are intrinsically different, both of which, however, can be prepared deterministically by engineering their directional properties. We then demonstrate that this feature provides the possibilities for both the Mollow spectral combinations to be able to exhibit temporal two-color bunching effects only for a specific two-photon detection order with large violations of classical inequality but completely different spatially two-point directional properties. In the light of these highly directional properties, the laser-dressed two-atom system is able to behavior as a subwavelength atomic antenna, namely, a highly directional time-ordered cascaded photon source for quantum spectroscopy, such as Mollow spectroscopy [32–34].

This paper is organized as follows. In Sec. II we introduce the theoretical model by describing the quantum master equation from the two-atom collective bare-state picture to the collective dressed-state picture. In Sec. III we analyze the connection between the time orderings and spatial directionality for different Mollow spectral combinations based on the obtained analytic formalism of the frequency-resolved intensity-intensity two-time correlations. We then discuss the geometric schemes for different Mollow spectral combinations to produce highly directional temporal two-color bunching effects and examine their nonclassical correlation properties. In Sec. IV we compare the subwavelength theoretical model we discussed with the Dicke model and atomic ensemble, and point out their connections and principal differences in photon statistics and directionality. Finally, in Sec. V we summarize our results and outline some possible further ideas based on this work.

II. THEORETICAL MODEL

We construct a quantum radiator which can be treated as a subwavelength atomic antenna with the most primitive

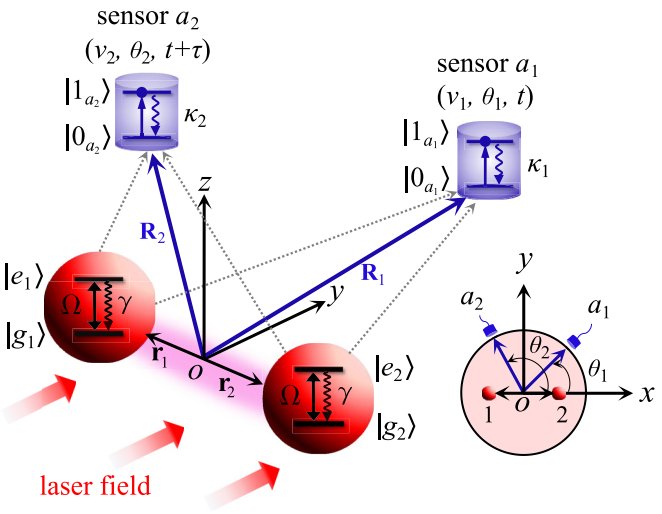

FIG. 1. Geometry of the theoretical model. The collective quantum radiator is composed of two identical two-level atoms, which are located at the positions $\mathbf{r}_1 = (-r_{12}/2, 0, 0)$ and $\mathbf{r}_2 = (r_{12}/2, 0, 0)$, respectively, and are illuminated by a strong laser field propagating in the y direction. The two-atom resonance fluorescence is resolved in far-field zone by two frequency-tunable two-level quantum sensors a_1 and a_2, located at the positions $\mathbf{R}_1$ and $\mathbf{R}_2$, respectively. The definitions of the two detection angles (θ_1, θ_2) in the x–y plane are labeled in the two-dimensional diagram

few-body geometric configuration. It is composed of two identical atoms located at their respective positions $\mathbf{r}_1 = (-r_{12}/2, 0, 0)$ and $\mathbf{r}_2 = (r_{12}/2, 0, 0)$ (see Fig. 1). Each of the atoms is modeled as a two-level system, which supports only an electric dipole transition between the excited state $|e_j\rangle$ and the ground state $|g_j\rangle (j \in \{1, 2\})$, separated by the transition frequency $\omega_j = \omega_0$ and connected by the spontaneous emission rates $\gamma_j = \gamma$. The two-atom system is pumped by a strong laser field of the frequency ω_L and the Rabi frequencies $\Omega(\mathbf{r}_j) = \Omega e^{i\mathbf{k}_L \cdot \mathbf{r}_j}$ with $\mathbf{k}_L$ being the wave vector of the laser field. If we consider a special driving configuration in which the direction of propagation of the driving laser field is perpendicular to the interatomic axis, $\mathbf{k}_L \cdot \mathbf{r}_{12} = 0$, the Rabi frequencies experienced by the spatially separated atoms can be equal and real, i.e., $\Omega(\mathbf{r}_j) = \Omega$ [35]. In practical terms, the subwavelength two-atom antenna can be realized by trapping two ultracold neutral atoms into separate potential wells of optical traps or optical lattice sites with relatively fixed positions but controllable interatomic distances [36–38]. In these situations, the atomic vibrations can be suppressed such that the trapped atoms can be treated as motionless with respect to the spatial scale of the order of an optical wavelength [39,40].

Our objective is to explore the spectrally resolved collective correlated emissions of the two-atom system. This prompts us to treat it in the Mollow regime, i.e., the strong driving-field limit. Thus it is more convenient to access the atomic emission dynamics by introducing the laser-atom dressed states [41]

$$|+_j\rangle = \cos\phi|e_j\rangle + \sin\phi|g_j\rangle, \tag{1a}$$

$$|-_j\rangle = \sin\phi|e_j\rangle - \cos\phi|g_j\rangle, \tag{1b}$$

where we have defined $\cos\phi$ and $\sin\phi = \sqrt{(\bar{\Omega} \pm \Delta_{\rm L})/2\bar{\Omega}}$ with $2\phi = \arctan(\Omega/\Delta_{\rm L})$, the effective Rabi frequency $\bar{\Omega} = \sqrt{\Omega^2 + \Delta_{\rm L}^2}$, and the detuning of the laser frequency from the atomic resonance $\Delta_{\rm L} = \omega_0 - \omega_{\rm L}$. For two-atom systems, we recognize that the extremely strong collective coherent coupling rate may alter the typical line shape of single-atom Mollow triplet [42]. However, it occurs only when the interatomic distance is much smaller than a resonant wavelength, giving rise to the divergence of Ω_{12}. Under such circumstances, the two-atom system is deprived of the directionality of our interest arising from the spatial phase factor $e^{i\mathbf{k}\cdot\mathbf{r}_{12}}$ [35]. If the two-atom system is able to operate as a highly directional atomic antenna, the linear dimension should be of the order of a resonant wavelength.

In the dressed-state picture, by tracing over the free-space electromagnetic vacuum reservoir, the master equation of the laser-dressed two-atom system is given by $\partial\rho/\partial t = \mathcal{L}_A\rho$ as follows:

$$\frac{\partial\rho}{\partial t} = -i\,[H_A,\,\rho] + \sum_{i,j=1}^{2}\big\{\Gamma_{ij}^{+}[R_{-}^{(i)}\rho,\,R_{+}^{(j)}] + \Gamma_{ij}^{-}[R_{+}^{(i)}\rho,\,R_{-}^{(j)}] + \Gamma_{ij}^{\rm L}\big[R_{z}^{(i)}\rho,\,R_{z}^{(j)}\big] + \text{H.c.}\big\}, \quad (2)$$

with the total Hamiltonian H_A including the free part and the effective coherent dipole-dipole interactions

$$H_A = \sum_{j=1}^{2}\bar{\Omega}R_{z}^{(j)} + \sum_{i\neq j=1}^{2}\big[\Delta_{ij}^{+}R_{+}^{(i)}R_{-}^{(j)} + \Delta_{ij}^{-}R_{-}^{(i)}R_{+}^{(j)} + \Delta_{ij}^{\rm L}R_{z}^{(i)}R_{z}^{(j)}\big]. \quad (3)$$

Here the dressed-state transition operators $R_{\pm}^{(j)} = |\pm_j\rangle\langle\mp_j|$ and $R_{z}^{(j)} = [|+_j\rangle\langle+_j| - |-_j\rangle\langle-_j|]/2$ can be considered as the sources of the left (L) and right (R) Rabi sidebands and the central (C) band of the single-atom Mollow triplet, respectively. The coefficients $\{\Delta_{ij}^{\pm}, \Delta_{ij}^{\rm L}\}$ and $\{\Gamma_{ij}^{\pm}, \Gamma_{ij}^{\rm L}\}$ are the effective coherent coupling rates and dissipative coupling rates between dressed-state transitions of different dressed atoms for $i \neq j$ or single-atom dressed-state decay rates for $i = j$, respectively, of different Mollow characteristic frequencies $\omega_{\rm L}$ and $\omega_{\pm} = \omega_{\rm L} \pm \bar{\Omega}$. These interatomic effective coupling rates and single-atom dressed-state decay rates are given by

$$\Delta_{ij}^{+} = \Omega_{ij}^{+}\cos^4\phi, \quad \Gamma_{ij}^{+} = \frac{\gamma_{ij}^{+}}{2}\cos^4\phi, \quad (4a)$$

$$\Delta_{ij}^{-} = \Omega_{ij}^{-}\sin^4\phi, \quad \Gamma_{ij}^{-} = \frac{\gamma_{ij}^{-}}{2}\sin^4\phi, \quad (4b)$$

$$\Delta_{ij}^{\rm L} = \Omega_{ij}^{\rm L}\sin^2(2\phi), \quad \Gamma_{ij}^{\rm L} = \frac{\gamma_{ij}^{\rm L}}{2}\sin^2(2\phi), \quad (4c)$$

where $\Omega_{ij}^{\alpha} = \Omega_{ij}(\omega_\alpha)$ and $\gamma_{ij}^{\alpha} = \gamma_{ij}(\omega_\alpha)$ are the bare interatomic coherent coupling rates (Ω_{ij}^{α}) and dissipative coupling rates ($\gamma_{ij}^{\alpha}, i \neq j$) or bare single-atom decay rates (γ_{jj}^{α}), respectively, which are now calculated at the Mollow dressed-state transition frequencies $\omega_\alpha = \omega_{\rm L}$ and $\omega_{\pm}$. These vacuum-induced rates are generally frequency-dependent. However, since we are working in free space, in which the density of the electromagnetic vacuum modes is slowly varying (an infinitely broad spectrum) around the atomic transition frequency (optical frequency for typical atomic systems [35]), these vacuum-induced rates at different Mollow dressed-state transition frequencies can be approximated as $\Omega_{ij}^{\alpha} = \Omega_{ij}$, $\gamma_{ij}^{\alpha} = \gamma_{ij}$ for $i \neq j$, and $\gamma_{11}^{\alpha} = \gamma_{22}^{\alpha} = \gamma$ [43]. For parallel electric dipole orientations of two atoms, the bare interatomic coherent and dissipative coupling rates in free space are connected by [24,27,35]

$$\Omega_{ij} + i\left(\frac{\gamma_{ij}}{2}\right) = \frac{3}{4}\gamma\left\{\frac{\cos^2\Theta - 1}{kr_{12}} + (1 - 3\cos^2\Theta) \times \left[\frac{i}{(kr_{12})^2} + \frac{1}{(kr_{12})^3}\right]\right\}e^{-ikr_{12}}, \quad (5)$$

where Θ is the angle between the parallel electric dipole moments $\mathbf{d}_j = \mathbf{d}$ and the interatomic distance vector $\mathbf{r}_{12} = \mathbf{r}_2 - \mathbf{r}_1$, which is set to $\pi/2$ in our geometry, and $k = 2\pi/\lambda$ is the wave number of the atomic radiation fields with the central wavelength λ. Note that the master equation (2) was obtained in the strong-field limit, i.e., $\bar{\Omega} \gg \{\gamma, \gamma_{12}, \Omega_{12}\}$, for which the subwavelength interatomic distances are necessary to ensure that $\{\Omega_{12}, \gamma_{12}\} \sim \gamma$. Under this condition, the master equation (2) transparently reveals that the photon exchange between two dressed atoms occurs only between resonant dressed-state transitions, whereas the nonresonant coupling terms with the rapidly oscillating frequencies $\bar{\Omega}$ and $2\bar{\Omega}$ have been neglected. This formalism gives rise to the effect of laser-induced dipole-dipole interactions that can still be described in terms of the resonant electric dipole-dipole interactions [44].

Regarding the frequency-resolving part, based on the sensor theory proposed in Ref. [45], we introduce a pair of quantum sensors in far-field zone at the positions $\mathbf{R}_1$ and $\mathbf{R}_2$, respectively. Each of the quantum sensors is modeled as a two-level bosonic system, and thus described by the annihilation operator $a_l = |0_{a_l}\rangle\langle 1_{a_l}|(l \in \{1, 2\})$ with the ground state $|0_{a_l}\rangle$ and the single-excitation state $|1_{a_l}\rangle$. The two energy levels of each quantum sensor are separated by the transition frequency ν_l, which is tuned to the central frequency of the Mollow spectral line to be resolved. Including the dissipation of the quantum sensors with the decay rates κ_l, the reduced density operator of the two-sensor system evolves according to its master equation $\partial\rho/\partial t = \mathcal{L}_F\rho$, which takes the form of

$$\frac{\partial\rho}{\partial t} = -i\sum_{l=1}^{2}[\Delta_l a_l^{\dagger}a_l,\,\rho] + \sum_{l=1}^{2}\frac{\kappa_l}{2}\{[a_l\rho,\,a_l^{\dagger}] + \text{H.c.}\}, \quad (6)$$

with the detunings of the quantum sensor modes $\Delta_l = \nu_l - \omega_{\rm L}$. In the following we assume $\kappa_l = \kappa$ for the sake of simplicity. Based on the spirit of the sensor method proposed by del Valle *et al.* [45], the quantum filtering dynamics can be described by the extremely weak coherent coupling between the quantum sensors and the photon modes emitted from the quantum emitter, so we therefore construct the photon frequency-filtering mechanism for our system through the filtering Hamiltonian

$$H_I = \sum_{l=1}^{2}\sum_{m=1}^{3} g_m\big(a_l^{\dagger}R_m^{[l]} + a_l R_m^{[l]\dagger}\big), \quad (7)$$

where the coefficients $g_1 = -g\cos^2\phi$, $g_2 = g\sin^2\phi$, and $g_3 = g\sin(2\phi)$ with $g \to 0$ are the effective coupling rates between the sensor modes and the emitted Mollow photons of the right Rabi sideband ($m = 1$), the left Rabi sideband ($m = 2$), and the central band ($m = 3$), respectively. Here $R_m^{[l]}$ are the collective radiation field operators responsible of the mth Mollow spectral line resolved by the sensor mode a_l, which take the form

$$R_1^{[l]} = R_-^{(1)} e^{ik|\mathbf{R}_l - \mathbf{r}_1|} + R_-^{(2)} e^{ik|\mathbf{R}_l - \mathbf{r}_2|}, \tag{8a}$$

$$R_2^{[l]} = R_+^{(1)} e^{ik|\mathbf{R}_l - \mathbf{r}_1|} + R_+^{(2)} e^{ik|\mathbf{R}_l - \mathbf{r}_2|}, \tag{8b}$$

$$R_3^{[l]} = R_z^{(1)} e^{ik|\mathbf{R}_l - \mathbf{r}_1|} + R_z^{(2)} e^{ik|\mathbf{R}_l - \mathbf{r}_2|}. \tag{8c}$$

One can notice that the spatial phase factors $e^{\pm ik|\mathbf{R}_l - \mathbf{r}_j|}$ of the electric dipole radiation fields enter the filtering Hamiltonian (7), which play a vital role in the engineering of directionality. By extending the Hilbert subspaces of the dressed two-atom system and the sensors to the dressed atom-sensor combined Hilbert space, we arrive at the master equation for the dressed atom-sensor combined density operator ρ,

$$\frac{\partial \rho}{\partial t} = -i[H_I, \rho] + \mathcal{L}_0 \rho, \tag{9}$$

with $\mathcal{L}_0 = \mathcal{L}_A + \mathcal{L}_F$. If we further perform the unitary dressing transformation for the filtering Hamiltonian (7), we obtain

$$\tilde{H}_I = \sum_{l=1}^{2} \left[g_1 a_l^\dagger R_1^{[l]} e^{i(\Delta_l - \bar{\Omega})t} + g_2 a_l^\dagger R_2^{[l]} e^{i(\Delta_l + \bar{\Omega})t} + g_3 a_l^\dagger R_3^{[l]} e^{i\Delta_l t} \right] + \text{H.c.} \tag{10}$$

The filtering Hamiltonian (10) is general in terms of the quantum sensor-laser detunings so that both the sensor modes can be either on resonance or off resonance with the three Mollow characteristic frequencies ω_L and $\omega_L \pm \bar{\Omega}$. Thus, the Hamiltonians (7) and (10) have covered all the possible two-color spectral combinations to be filtered. In the following, we consider the case of resonant filtering by tuning the frequencies of both the sensors to be on resonance with the central frequencies of their respective target Mollow spectral lines for different spectral combinations, i.e., $(\Delta_1, \Delta_2) = (\bar{\Omega}, 0)$ or $(\bar{\Omega}, -\bar{\Omega})$. Under each specific resonance tuning of the sensors to the dressed-state transition frequencies, the rapidly oscillating terms of far off-resonance in the filtering Hamiltonian (10) with the oscillating frequencies $\bar{\Omega}$ and $2\bar{\Omega}$ can be discarded.

The spirit of sensor method lies in the vanishing back action from quantum sensors to quantum emitter, giving rise to the weak single-excitation of each quantum sensor mode. Thus the frequency-resolved N-photon intensity-intensity correlation functions are of the order of g^{2N}, as pointed out in the perturbation approach of frequency-resolved photon correlations in Ref. [46]. We thus expand the total density operator of the dressed atom-sensor combined system with respect to the weak coupling rate g as $\rho = \rho^{(0)} + \rho^{(1)} + \rho^{(2)} + \cdots$, in which the zeroth-order solution $\rho^{(0)}$ and the correction term of each order $[\rho^{(1)}, \rho^{(2)}, \ldots]$ are, respectively, governed by the equations of motion

$$\frac{\partial \rho^{(0)}}{\partial t} = \mathcal{L}_0 \rho^{(0)}, \tag{11a}$$

$$\frac{\partial \rho^{(n)}}{\partial t} = \mathcal{L}_0 \rho^{(n)} - i[H_I, \rho^{(n-1)}], \quad (n \geqslant 1), \tag{11b}$$

which serve as the starting point of calculating the frequency-time-resolved photon correlation functions. In order to gain insight into the radiative dynamics of the dressed two-atom system more thoroughly, it is more convenient to further introduce the two-atom superposed dressed basis $|1(4)_A\rangle = |\pm_1\rangle|\pm_2\rangle$ and $|2(3)_A\rangle = [|+_1\rangle|-_2\rangle \pm |-_1\rangle|+_2\rangle]/\sqrt{2}$. In this case the dressed two-atom system is transformed as four decoupled dressed quantum emitters weighted by the steady-state populations $\rho_{kk} (k \in \{1, 2, 3, 4\})$, which are the zeroth-order steady-state solution of Eq. (11a). However, the quantum filtering dynamics described by Eq. (11b) cannot be classified, in general, according to the diagonalized dressed states. This is due to the fact that each sensor is weakly excited by the emitted Mollow photons of same central frequency that may be generated from the transitions triggered by different diagonalized dressed states. However, the physical insight in this situation can still be probed transparently if the timescale we concentrate on is comparable to the lifetime of the sensors ($\tau \sim \kappa^{-1}$) but much smaller than the timescale of the atomic radiative dynamics ($\sim\gamma^{-1}$), i.e., the condition of broad filtering passband $\kappa \gg \gamma$ [47,48]. Such a timescale is usually necessary for the spectral resolution of resonance fluorescence with a multipeak line shape generated by a strong driving laser field, which ensures that all the photons from the target spectral line are sampled into the spectrometer with equal probability [47,48]. Even for a more general situation in which the filtering bandwidth is comparable with atomic linewidth, the physical pictures revealed by the broad-filtering case are also instructive [49–51].

III. SPACE-TIME PHOTON CORRELATIONS WITH TWO-COLOR TIME ORDERINGS

Let us consider the problem that a Mollow photon of frequency ν_1 is detected at the time t in the direction θ_1 and how the emission of the another Mollow photon of different frequency ν_2 depends not only on the direction θ_2 but also on the time delay τ. At the same time, we intend to explore the crucial role of time orderings of Mollow cascaded emission in this problem. The frequency-time-resolved two-photon intensity-intensity correlation function of the dressed two-atom system is defined as

$$g_{12}^{(2)}(\theta_1, 0; \theta_2, \tau) = \frac{G_{12}^{(2)}(\theta_1, 0; \theta_2, \tau)}{G_1^{(1)}(\theta_1) G_2^{(1)}(\theta_2)}, \tag{12}$$

where $G_{12}^{(2)}(\theta_1, 0; \theta_2, \tau) = \langle : a_1^\dagger(t) a_2^\dagger(t+\tau) a_2(t+\tau) a_1(t) : \rangle$ is the unnormalized intensity-intensity correlation in terms of the sensor modes, and $G_l^{(1)}(\theta_l) = \langle a_l^\dagger a_l \rangle (l \in \{1, 2\})$ are the single-photon filtered radiation intensities resolved by the sensor modes a_l. Here the azimuth functions that describe the angular pattern of single-atom electric dipole radiation pattern $u(\vartheta_l) = (3\pi/8)\sin^2\vartheta_l$ depending on the angle ϑ_l between the direction of observation and the direction of the atomic dipole

TABLE I. Directional functions controlling the two-photon correlation components $|\mathcal{C}_j^{(k)}(\tau)|^2$ between the right Rabi sideband and the central band (R, C) for positive and reverse time orderings in the cases of positive and negative time delays. The two-photon cascaded emissions $|k_A\rangle \xrightarrow{a_1} |k'_A\rangle \xrightarrow{a_2} |j_A\rangle$ or $|k_A\rangle \xrightarrow{a_2} |k'_A\rangle \xrightarrow{a_1} |j_A\rangle$ are indicated by the corresponding final-state two-photon probability amplitude $\mathcal{C}_j^{(k)}(\tau)$.

Two-photon channel	Positive (Reverse) time ordering for $\tau > 0 (\tau < 0)$	Reverse (Positive) time ordering for $\tau > 0 (\tau < 0)$	Time-ordering interference
$\|\mathcal{C}_2^{(1)}(\tau)\|^2$	$(1+\cos\eta_1)(1-\cos\eta_2)$	$(1-\cos\eta_1)(1+\cos\eta_2)$	$-2\sin\eta_1\sin\eta_2$
$\|\mathcal{C}_3^{(1)}(\tau)\|^2$	$(1-\cos\eta_1)(1-\cos\eta_2)$	$(1+\cos\eta_1)(1+\cos\eta_2)$	$2\sin\eta_1\sin\eta_2$
$\|\mathcal{C}_4^{(2)}(\tau)\|^2$	$(1-\cos\eta_1)(1+\cos\eta_2)$	$(1+\cos\eta_1)(1-\cos\eta_2)$	$-2\sin\eta_1\sin\eta_2$
$\|\mathcal{C}_4^{(3)}(\tau)\|^2$	$(1+\cos\eta_1)(1+\cos\eta_2)$	$(1-\cos\eta_1)(1-\cos\eta_2)$	$2\sin\eta_1\sin\eta_2$

moments have been absorbed into the effective coupling coefficients g_m, which vanish algebraically in the normalized correlation functions. Nevertheless, we assume that the atomic dipole moments are all oriented perpendicular to the detection plane, i.e., $\vartheta_l = \pi/2$. Furthermore, it is sufficient to explore the directionality by restricting our discussion to the case of $|\mathbf{R}_1| = |\mathbf{R}_2|$, which means that the distances from the far-field observation points to the coordinate origin are irrelevant.

A. Space-time photon correlations between sideband and central band

We first examine the frequency-time-resolved two-photon correlated emission between the central (C) band and the right (R) Rabi sideband. Assuming that the sensor mode a_1 resolves a Mollow photon from the right Rabi sideband at a given time t, the conditional event of detecting another Mollow photon from the central band resolved by the sensor mode a_2 at the time $t+\tau$ is described by the two-time correlation function $G^{(2)}_{\mathrm{RC}}(\theta_1, 0; \theta_2, \tau)$. Based on the perturbation master equations (11a) and (11b) up to the second order and under the condition of broad filtering, the analytic form of $G^{(2)}_{\mathrm{RC}}(\theta_1, 0; \theta_2, \tau)$ is calculated as

$$G^{(2)}_{\mathrm{RC}}(\theta_1, 0; \theta_2, \tau) = \rho_{11}\left[\left|\mathcal{C}_2^{(1)}(\tau)\right|^2 + \left|\mathcal{C}_3^{(1)}(\tau)\right|^2\right] + \rho_{22}\left|\mathcal{C}_4^{(2)}(\tau)\right|^2 + \rho_{33}\left|\mathcal{C}_4^{(3)}(\tau)\right|^2. \quad (13)$$

Here $\mathcal{C}_2^{(1)}(\tau)$, $\mathcal{C}_3^{(1)}(\tau)$, $\mathcal{C}_4^{(2)}(\tau)$, and $\mathcal{C}_4^{(3)}(\tau)$ can be regarded as the two-photon probability amplitudes, with the following analytic forms for positive time delay ($\tau > 0$):

$$\begin{aligned}
\mathcal{C}_2^{(1)}(\tau) &= g_{23}g_{31}\mathcal{F}^{(+)}_{1\to2}(\tau) + g_{21}g_{11}\mathcal{F}^{(-)}_{1\to2}(\tau),\\
\mathcal{C}_3^{(1)}(\tau) &= g_{32}g_{21}\mathcal{F}^{(+)}_{1\to2}(\tau) + g_{31}g_{11}\mathcal{F}^{(-)}_{1\to2}(\tau),\\
\mathcal{C}_4^{(2)}(\tau) &= g_{44}g_{42}\mathcal{F}^{(+)}_{1\to2}(\tau) + g_{43}g_{32}\mathcal{F}^{(-)}_{1\to2}(\tau),\\
\mathcal{C}_4^{(3)}(\tau) &= g_{44}g_{43}\mathcal{F}^{(+)}_{1\to2}(\tau) + g_{42}g_{23}\mathcal{F}^{(-)}_{1\to2}(\tau), \quad (14)
\end{aligned}$$

respectively, whereas the corresponding analytic forms for negative time delay ($\tau < 0$) turn out to be only the replacement of $\mathcal{F}^{(+)}_{1\to2}(\tau)$ and $\mathcal{F}^{(-)}_{1\to2}(\tau)$ in Eq. (14) with $\mathcal{F}^{(-)}_{2\to1}(\tau)$ and $\mathcal{F}^{(+)}_{2\to1}(\tau)$, respectively, with $\tau < 0$. For positive time delay, we have introduced the two-photon cascaded emission amplitudes of positive time ordering $\mathcal{F}^{(+)}_{1\to2}(\tau)$ and reverse time ordering $\mathcal{F}^{(-)}_{1\to2}(\tau)$. Correspondingly, $\mathcal{F}^{(+)}_{2\to1}(\tau)$ and $\mathcal{F}^{(-)}_{2\to1}(\tau)$ are the two-photon cascaded emission amplitudes of positive time ordering and reverse time ordering for negative time delay. The order of their subscripts from left to right ($1\to2$ and $2\to1$) indicates the detection order of the sensor modes a_1 and a_2. Their analytic forms are given by

$$\mathcal{F}^{(+)}_{1\to2(2\to1)}(\tau) = \frac{-i}{\Gamma_1\Gamma_2}\left[1 - \frac{\Gamma_{1(2)}}{\Gamma_1+\Gamma_2}e^{-\Gamma_{2(1)}|\tau|}\right], \quad (15a)$$

$$\mathcal{F}^{(-)}_{1\to2(2\to1)}(\tau) = \frac{-i}{\Gamma_{2(1)}(\Gamma_1+\Gamma_2)}e^{-\Gamma_{2(1)}|\tau|}, \quad (15b)$$

where we have abbreviated $\Gamma_l = \frac{\kappa}{2} + i\delta_l$ with $\delta_1 = \Delta_1 - \bar{\Omega} = \nu_1 - \omega_+$ and $\delta_2 = \Delta_2 = \nu_2 - \omega_{\mathrm{L}}$ being the detunings of the quantum sensor modes a_1 and a_2, respectively, from the central frequencies of their respective target spectral lines. For positive time delay, the two-photon cascaded emission amplitude of positive time ordering $\mathcal{F}^{(+)}_{1\to2}(\tau)$ describes the physical situation in which the order of two-photon cascaded emission $|k_A\rangle \xrightarrow{a_1} |k'_A\rangle \xrightarrow{a_2} |j_A\rangle$ corresponds to the two-photon delayed detection order, i.e., $a_1 \to a_2$, whereas the reverse one $\mathcal{F}^{(-)}_{1\to2}(\tau)$ describes the opposite situation, i.e., the first detected photon resolved by the sensor mode a_1 in the detection order $a_1 \to a_2$ is emitted later in the cascaded emission $|k_A\rangle \xrightarrow{a_2} |k'_A\rangle \xrightarrow{a_1} |j_A\rangle$. Regarding negative time delay, the orders of two-photon cascaded emission described by $\mathcal{F}^{(\pm)}_{2\to1}(\tau)$ are just opposite to those of positive time delay. One can see from Eq. (14) that the two-photon cascaded emission amplitudes of time orderings $\mathcal{F}^{(\pm)}_{1\to2}(\tau)$ and $\mathcal{F}^{(\pm)}_{2\to1}(\tau)$ construct the analytic framework of the two-photon amplitude $\mathcal{C}_j^{(k)}(\tau)$ with the form of quantum interference between opposite time orderings. They are modulated by the direction-dependent right-sideband effective coupling rates $g_{42} = -g_{21} = g_2\chi_-$, $g_{43} = g_{31} = -g_2\chi_+$, and the central-band effective coupling rates $g_{11} = -g_{44} = (g_1\chi_+)/\sqrt{2}$, $g_{23} = g_{32} = (-g_1\chi_-)/\sqrt{2}$, where $\chi_\pm = (e^{i\mathbf{k}\cdot\mathbf{r}_1} \pm e^{i\mathbf{k}\cdot\mathbf{r}_2})/\sqrt{2}$ are the far-field spatial interference factors with $\eta_l = \mathbf{k}_l \cdot \mathbf{r}_{12} = kr_{12}\cos\theta_l$. In order to gain insight into the underlying physical mechanisms of direction-dependent time orderings, we further analyze the obtained short time-delay analytic formalism in Eqs. (13)–(15b), which allows us to calculate four directional functions $\Theta_j^{(k)}(\theta_1, \theta_2) = \Theta_\pm(\theta_1)\Theta_\pm(\theta_2)$ listed in Table I, where $\Theta_\pm(\theta_l) = 1 \pm \cos\eta_l$. Mathematically, these directional functions are the prefactors of $|\mathcal{F}^{(\pm)}_{1\to2}(\tau)|^2$ and $|\mathcal{F}^{(\pm)}_{2\to1}(\tau)|^2$ when calculating the two-photon probability component $|\mathcal{C}_j^{(k)}(\tau)|^2$. For completeness, the directional functions responsible for the quantum interference between positive time ordering and reverse time ordering are also listed in Table I.

The temporal features of $g^{(2)}_{\rm RC}(\theta_1, 0; \theta_2, \tau)$ are shown by its analytic solutions and numerical solutions for the cases of exactly resonant driving in Fig. 2(a) and large laser detuning in Fig. 2(c), in which the relevant correlation components triggered by the predominant dressed states (steady-state dressed populations) are also analyzed in Figs. 2(b) and 2(d) with the help of the short time-delay analytic solutions in Eq. (13). In Figs. 2(a) and 2(c), both the analytical solutions and numerical solutions of arbitrary time delay are calculated from the perturbation master equations (11a) and (11b), but the former and the latter are obtained by ignoring and considering the atomic decay rates, respectively, in the higher-order perturbation master equation (11b) in the case of broad filtering.

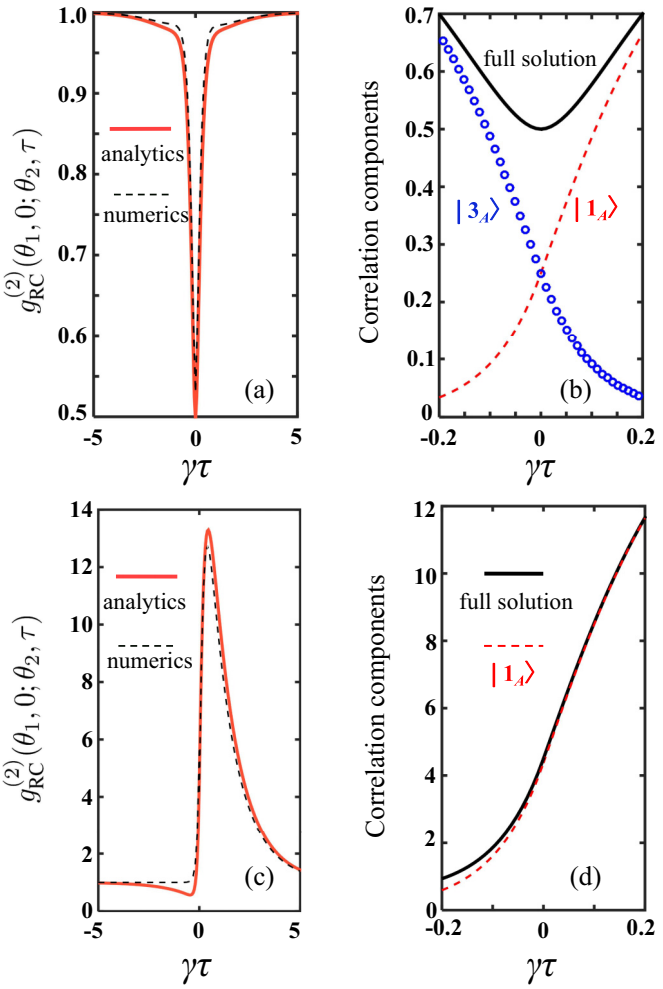

FIG. 2. Two-photon correlation $g^{(2)}_{\rm RC}(\theta_1, 0; \theta_2, \tau)$ and the corresponding correlation components. (a), (b) Two-photon correlations for $\Delta_{\rm L} = 0$ and $(\theta_1, \theta_2) = (0, \pi)$. (c), (d) Two-photon correlations for $\Delta_{\rm L} = -100\gamma$ and $(\theta_1, \theta_2) = (\pi/2, 0)$. Other parameters are $\Omega = 100\gamma$, $\kappa = 10\gamma$, $\delta_1 = 0$, $\delta_2 = 0$, and $r_{12} = \lambda/2$. (a), (c) Comparison of the analytic solutions of arbitrary time delay (red solid lines) with broad filtering approximation and the numerical solutions of arbitrary time delay (black dashed lines) with the spontaneous decay rates of the atoms being considered in Eq. (11b). (b), (d) Components of the full value of $g^{(2)}_{\rm RC}(\theta_1, 0; \theta_2, \tau)$ (black solid lines) triggered by the dressed states $|1_A\rangle$ (red dashed lines) and $|3_A\rangle$ (blue circular lines).

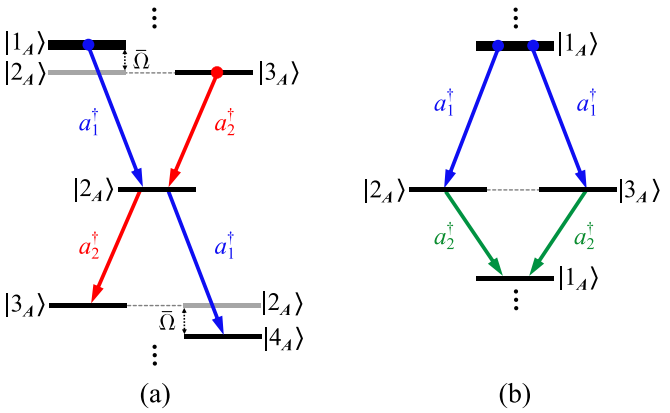

FIG. 3. Energy-level scheme of two-photon cascaded emissions in the dressed-state picture. (a) Two-photon cascaded emissions of the right-sideband photons (blue arrows) and the central-band photons (red arrows) resolved by the sensor modes a_1 and a_2, respectively, in the direction combinations $(\theta_1, \theta_2) = (0, 0)$, $(0, \pi)$, $(\pi, 0)$, and (π, π) for the interatomic distance $r_{12} = \lambda/2$. Time orderings are presented in the form of incoherent superposition between the positive time ordering triggered by the dressed state $|1_A\rangle$, in which the dressed two-atom system is predominantly trapped, and the reverse time ordering triggered by the dressed state $|3_A\rangle$. (b) Two-photon cascaded emissions of the right-sideband photons (blue arrows) and the left-sideband photons (green arrows) resolved by the sensor modes a_1 and a_2, respectively, triggered by the predominant dressed state $|1_A\rangle$. The two-channel quantum interference between positive time orderings are established.

In order to analyze the relationship between the structure of time orderings and temporal photon statistics, let us first examine the case of resonant driving, $\Delta_{\rm L} = 0$. In this circumstance, the distribution of time orderings is fully displayed by all the evenly populated dressed states that trigger them. One can see from Table I that each directional function controls both positive and reverse time orderings triggered by different dressed states. This suggests that, for a given detection order, an isolated time ordering cannot be achieved for resonant driving, leading to the symmetry of temporal photon statistics, as shown in Fig. 2(a). Specifically, it can be checked from Table I that, for $r_{12} = \lambda/2$, all the two-photon cascaded emission channels are spatially suppressed at four direction combinations $(\theta_1, \theta_2) = (0, 0)$, $(0, \pi)$, $(\pi, 0)$, and (π, π) due to $\cos\eta_1 = \cos\eta_2 = -1$, except for the pair of temporally antisymmetric channels $|1_A\rangle \xrightarrow{a_1} |2_A\rangle \xrightarrow{a_2} |3_A\rangle$ described by $\mathcal{C}_3^{(1)}(\tau)$ and $|3_A\rangle \xrightarrow{a_2} |2_A\rangle \xrightarrow{a_1} |4_A\rangle$ described by $\mathcal{C}_4^{(3)}(\tau)$, as sketched in Fig. 3(a). These two cascaded emissions channels behave as each other's reverse time orderings with the form of incoherent superposition irrespective of detection orders, and their contributions to the full two-photon statistics are extracted in Fig. 2(b). Obviously, this is in contrast to the case of single-atom Mollow triplet where, for resonant driving, the completely destructive interference of antisymmetric time orderings between one of the Rabi sidebands and the central band gives rise to the complete antibunching effect $g^{(2)}_{\rm RC} = 0$ for isochronous detection [47,48,51].

If the atomic population is approximately trapped in a specific dressed state, the situation is intrinsically different

from that of evenly triggered time orderings, as shown in Fig. 2(c). Here we should point out that it has been noticed in Ref. [52] that a specific time ordering of single-atom Mollow triplet can be protruded by approximately trapping the dressed atom in a single dressed state via large laser detuning. This foundational dressed-state radiative dynamics serves as the first step in our scheme to prepare desired time ordering. Considering that the dressed-state transitions generating the right Rabi sideband cannot be triggered by the collective lower dressed state $|4_A\rangle$, we thus enforce the dressed two-atom system via properly detuned driving laser to emit preferentially from the dressed state $|1_A\rangle$. Consequently, only the probability amplitudes $\mathcal{C}_2^{(1)}(\tau)$ and $\mathcal{C}_3^{(1)}(\tau)$ with the relevant directional functions in Table I are privileged, predominantly contributing to the full two-photon statistics as shown in Fig. 2(d). In view of the fact that the directional properties of this group of two-mode photon pair are completely separated such that $\Theta_j^{(k)}(\theta_1,\theta_2)=\Theta_\pm(\theta_1)\Theta_\pm(\theta_2)$, we can determine the geometric conditions of the two quantum sensors respectively to control the temporal two-color photon statistics. For positive time delay, the geometric conditions to achieve enhancement of only positive time ordering and thus strong bunching effect only for positive time delay are determined by

$$\frac{\partial\Theta_\pm(\theta_1)}{\partial\theta_1}=0 \quad \text{and} \quad \frac{\partial^2\Theta_\pm(\theta_1)}{\partial\theta_1^2}<0, \tag{16a}$$

$$\frac{\partial\Theta_-(\theta_2)}{\partial\theta_2}=0 \quad \text{and} \quad \frac{\partial^2\Theta_-(\theta_2)}{\partial\theta_2^2}<0, \tag{16b}$$

for the sensor modes a_1 and a_2, respectively, or equivalently

$$\theta_1=n_1\pi, \tag{17a}$$

$$\text{or} \quad \cos\theta_1=n_1\frac{\lambda}{2r_{12}}, \tag{17b}$$

for the sensor mode a_1 with $n_1\in\{0,\pm1,\pm2,\ldots\}$, and

$$\theta_2=n_2\pi, \tag{18a}$$

$$\text{or} \cos\theta_2=\left(n_2+\frac{1}{2}\right)\frac{\lambda}{r_{12}}, \tag{18b}$$

for the sensor mode a_2 with $n_2\in\{0,\pm1,\pm2,\ldots\}$. Here in addition to the conditions of principal maximum of the two-photon probability component $|\mathcal{C}_2^{(1)}(\tau)|^2$ or $|\mathcal{C}_3^{(1)}(\tau)|^2$ given by Eqs. (17b) and (18b), the distance-independent conditions (17a) and (18a) are also considered to determine the secondary maximum, especially when the condition of principal maximum (18b) cannot be satisfied if $r_{12}<\lambda/2$. Obviously, conditioned on the angular combinations (θ_1,θ_2) determined by Eqs. (17b) and (18b), if the detection order is reversed, i.e., for negative time delay, only reverse time ordering can be probed. This means that the privileged time ordering can be deterministically prepared. Similarly, for negative time delay, the conditions to achieve the enhancement of only positive time ordering are still given by Eq. (16a) or Eqs. (17a) and (17b), but the corresponding conditions for the sensor mode a_2 are now determined by

$$\frac{\partial\Theta_+(\theta_2)}{\partial\theta_2}=0 \quad \text{and} \quad \frac{\partial^2\Theta_+(\theta_2)}{\partial\theta_2^2}<0, \tag{19}$$

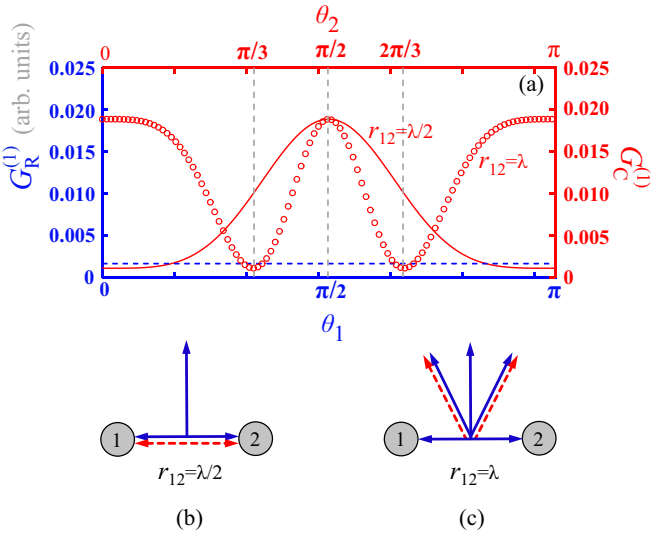

FIG. 4. (a) Angular distribution of the radiation intensities $G_R^{(1)}(\theta_1)$ and $G_C^{(1)}(\theta_2)$ for the laser detuning $\Delta_L=-100\gamma$. The blue dashed line corresponds to $G_R^{(1)}(\theta_1)$, and its direction-independent feature is persisted to the variation of the subwavelength interatomic distance $r_{12}(\sim\lambda)$. The red solid line and red circular line correspond to $G_C^{(1)}(\theta_2)$ for $r_{12}=\lambda/2$ and λ, respectively. All the other parameters are the same as in Fig. 2. (b), (c) Angular distribution and combination of $g_{RC}^{(2)}(\theta_1,0;\theta_2,\tau)$ for (b) $r_{12}=\lambda/2$ and (c) $r_{12}=\lambda$ at which the strong bunching effect only for positive time delay as shown in Fig. 2(c) can be achieved. The blue solid arrows and red dashed arrows represent the emission directions of the right-sideband photons and central-band photons, respectively.

or equivalently

$$\theta_2=n_2\pi, \tag{20a}$$

$$\text{or} \cos\theta_2=n_2\frac{\lambda}{r_{12}}, \tag{20b}$$

with $n_2\in\{0,\pm1,\pm2,\ldots\}$. However, whether the bunching effect can be effectively prepared in each angular combination determined by Eqs. (18b) and (20b) requires us to further check the angular distribution of single-photon filtered radiation intensities, i.e., the first-order field correlations. Figure 4(a) presents the single-side $(0\leqslant\theta_1,\theta_2\leqslant\pi)$ angular distribution of $G_R^{(1)}(\theta_1)$ and $G_C^{(1)}(\theta_2)$ under detuned driving, from which we can observe that the radiation intensity of the Rabi sideband photons [blue dashed line in Fig. 4(a)] is drastically insensitive to the spatial directionality in contrast to that of the central-band photons [red solid line and red circular line in Fig. 4(a)]. For $r_{12}=\lambda/2$, the spatially destructive interference of single-photon emission of central-band photons occurs along the atomic axis, i.e., the directions $\theta_2=0$ and π [see red solid line in Fig. 4(a)], which are just coincident with the condition of principal maximum (18b), whereas the directions of principal maximum predicted by Eq. (20b) for $r_{12}=\lambda/2$ are perpendicular to the atomic axis, i.e., the directions $\theta_2=\pi/2$ and $3\pi/2$, corresponding to the relatively strong directional focusing of single-photon emissions [see red solid line in Fig. 4(a)] and thus weak two-photon correlated emissions. Correspondingly, three directions of principal maximum for the sensor mode a_1 to

achieve strong bunching effect can be predicted at $\theta_1 = 0,\ \pi,\ \pi/2$, and $3\pi/2$, of which the angular combinations $(\theta_1, \theta_2) = (\pi/2, 0), (\pi/2, \pi), (3\pi/2, 0)$, and $(3\pi/2, \pi)$ are also generated from the incoherent superposition between the two-photon cascaded emission channels $|1_A\rangle \xrightarrow{a_1} |3_A\rangle \xrightarrow{a_2} |2_A\rangle$ and $|2_A\rangle \xrightarrow{a_2} |3_A\rangle \xrightarrow{a_1} |4_A\rangle$ with opposite time orderings. Obviously, this is similar to the cases of $(\theta_1, \theta_2) = (0, 0), (0, \pi), (\pi, 0)$, and (π, π) corresponding to Fig. 3(a). The optimum single-side angular combinations are sketched in Figs. 4(b) and 4(c) for $r_{12} = \lambda/2$ and λ, respectively, to achieve significant asymmetry of temporal photon statistics and strong two-color bunching effect only for positive time delay. Note that the emergence of the two extra directions of the sensor mode a_2 at $\theta_2 = \pi/3$ and $2\pi/3$ in Fig. 4(c) (blue arrows) is not only predicted by Eq. (18b), but also due to the suppression of single-photon emissions, as demonstrated in Fig. 4(a) (red circular line).

B. Space-time photon correlations between sidebands

We now proceed to correlate the Mollow photons from the right (R) Rabi sideband and the left (L) Rabi sideband at different space-time points. For the sake of consistency, positive time delay corresponds to the detection of a left-sideband photon resolved by the sensor mode a_2 at the time $t + \tau$ conditioned on the detection of a right-sideband photon resolved by the sensor mode a_1 at the earlier time t, while negative time delay corresponds to the reverse detection order. The perturbation master equations (11a) and (11b) in the case of broad filtering enable us to analyze the space-time quantum characteristics of $G^{(2)}_{\rm RL}(\theta_1, 0; \theta_2, \tau)$ by its analytic solution

$$\begin{aligned} G^{(2)}_{\rm RL}(\theta_1, 0; \theta_2, \tau) = {} & \rho_{11}\left|\mathcal{C}^{(1)}_1(\tau)\right|^2 + \rho_{44}\left|\mathcal{C}^{(4)}_4(\tau)\right|^2 \\ & + \rho_{22}\left[\left|\mathcal{C}^{(2)}_2(\tau)\right|^2 + \left|\mathcal{C}^{(2)}_3(\tau)\right|^2\right] \\ & + \rho_{33}\left[\left|\mathcal{C}^{(3)}_2(\tau)\right|^2 + \left|\mathcal{C}^{(3)}_3(\tau)\right|^2\right]. \end{aligned} \tag{21}$$

As we expected, its symmetric analytic structure is the embodiment of the physical equivalence of the dressed-state transitions of opposite Rabi sidebands. In the language of the two-photon cascaded emission amplitudes of positive and reverse time orderings introduced in Eqs. (15a) and (15b), the two-photon probability amplitudes in Eq. (21) for positive time delay ($\tau > 0$) are solved as

$$\begin{aligned} \mathcal{C}^{(1)}_1(\tau) &= g_{12}g_{21}\mathcal{F}^{(+)}_{1\to2}(\tau) + g_{13}g_{31}\mathcal{F}^{(+)}_{1\to2}(\tau), \\ \mathcal{C}^{(2)}_2(\tau) &= g_{24}g_{42}\mathcal{F}^{(+)}_{1\to2}(\tau) + g_{21}g_{12}\mathcal{F}^{(-)}_{1\to2}(\tau), \\ \mathcal{C}^{(2)}_3(\tau) &= g_{34}g_{42}\mathcal{F}^{(+)}_{1\to2}(\tau) + g_{31}g_{12}\mathcal{F}^{(-)}_{1\to2}(\tau), \\ \mathcal{C}^{(3)}_2(\tau) &= g_{24}g_{43}\mathcal{F}^{(+)}_{1\to2}(\tau) + g_{21}g_{13}\mathcal{F}^{(-)}_{1\to2}(\tau), \\ \mathcal{C}^{(3)}_3(\tau) &= g_{34}g_{43}\mathcal{F}^{(+)}_{1\to2}(\tau) + g_{31}g_{13}\mathcal{F}^{(-)}_{1\to2}(\tau), \\ \mathcal{C}^{(4)}_4(\tau) &= g_{42}g_{24}\mathcal{F}^{(-)}_{1\to2}(\tau) + g_{43}g_{34}\mathcal{F}^{(-)}_{1\to2}(\tau), \end{aligned} \tag{22}$$

where the analytic forms of $\mathcal{F}^{(+)}_{1\to2}(\tau)$ and $\mathcal{F}^{(-)}_{1\to2}(\tau)$ are still given by Eqs. (15a) and (15b), but the sensor detuning δ_2 should be redefined as $\delta_2 = \Delta_2 + \bar{\Omega} = \nu_2 - \omega_-$ due to the near-resonance tuning of the sensor mode a_2 to the left Rabi sideband. Correspondingly, the probability amplitudes for negative time delay can still be obtained straightforwardly by replacing $\mathcal{F}^{(+)}_{1\to2}(\tau)$ and $\mathcal{F}^{(-)}_{1\to2}(\tau)$ in Eq. (22) with $\mathcal{F}^{(-)}_{2\to1}(\tau)$ and $\mathcal{F}^{(+)}_{2\to1}(\tau)$, respectively. One can notice clearly from Eq. (22) that $\mathcal{C}^{(2)}_2(\tau), \mathcal{C}^{(2)}_3(\tau), \mathcal{C}^{(3)}_2(\tau)$, and $\mathcal{C}^{(3)}_3(\tau)$ have the common analytic framework as in Eq. (14), i.e., the quantum interference between positive time ordering and reverse time ordering. However, the other two, $\mathcal{C}^{(1)}_1(\tau)$ and $\mathcal{C}^{(4)}_4(\tau)$, are given by the quantum interference of same time orderings, such as the quantum interference between the positive time orderings $|1_A\rangle \xrightarrow{a_1} |2_A\rangle \xrightarrow{a_2} |1_A\rangle$ and $|1_A\rangle \xrightarrow{a_1} |3_A\rangle \xrightarrow{a_2} |1_A\rangle$, as sketched in Fig. 3(b). This is in contrast to the previous group of photon pair (R, C). The explicit forms of the left-sideband effective coupling rates are given by $g_{24} = -g_{12} = g_3\chi_-$ and $g_{13} = g_{34} = -g_3\chi_+$. The directional functions responsible for the angular properties of each correlation component in Eq. (21) are listed in Table II, in which the new directional function $\Theta^{(1)+}_1(\theta_1, \theta_2) = \Theta^{(4)-}_4(\theta_1, \theta_2) = 2 + 2\cos(\eta_1 + \eta_2)$, compared with Table I, is the consequence of the quantum interference between the two-photon cascaded channels with same time orderings.

We first consider the case of resonant laser driving to probe the full distribution of time orderings in this group of Mollow spectral combination. In order to reveal the contributions of the new directional function to the full two-photon intensity-intensity correlation, which arise from the time orderings triggered by the dressed states $|1_A\rangle$ and $|4_A\rangle$, we may consider the geometric conditions that maximize the new directional function $\Theta(\theta_1, \theta_2) = \cos(\eta_1 + \eta_2)$. For a given detection angle θ_1, the geometric conditions are given by

$$\frac{\partial\Theta(\theta_1, \theta_2)}{\partial\theta_2} = 0 \quad \text{and} \quad \frac{\partial^2\Theta(\theta_1, \theta_2)}{\partial\theta_2^2} < 0, \tag{23}$$

or equivalently

$$\theta_2 = n_2\pi, \tag{24a}$$

$$\text{or } \cos\theta_1 + \cos\theta_2 = n_2\frac{\lambda}{r_{12}}, \tag{24b}$$

under which the secondary maximum of the new directional function $\Theta(\theta_1, \theta_2)$ and the principal maximum $\Theta(\theta_1, \theta_2) = 1$ can be achieved, respectively. One can see that Eq. (24b) allows the two detection angles to be tuned continuously. Figure 5(a) shows the strictly symmetric temporal behavior of the two-color photon statistics $g^{(2)}_{\rm RL}(\theta_1, 0; \theta_2, \tau)$ of arbitrary delay for $\Delta_{\rm L} = 0$, $r_{12} = \lambda/2$, and a possible angular combination $(\theta_1, \theta_2) = (0, \pi)$, in which the analytic solution [red solid line in Fig. 5(a)] and numerical solution [black dashed line in Fig. 5(a)] are compared. In the short delay region, two pronounced temporal correlation peaks can be observed clearly, which are the consequence of the positive time orderings triggered by the dressed states $|1_A\rangle$ and $|4_A\rangle$ respectively. This can be demonstrated in Fig. 5(b) by splitting $g^{(2)}_{\rm RL}(\theta_1, 0; \theta_2, \tau)$ into four correlation components in short delay region according to the dressed populations with the help of the short-delay analytic solution given by Eq. (21). It can be seen clearly that the temporal characteristics of $g^{(2)}_{\rm RL}(\theta_1, 0; \theta_2, \tau)$ are completely determined by the incoherent superposition of the time orderings triggered by the dressed states $|1_A\rangle$ and $|4_A\rangle$, whereas the direction dependence of time orderings triggered by the other two dressed states disap-

TABLE II. Directional functions controlling the two-photon correlation components $|\mathcal{C}_j^{(k)}(\tau)|^2$ between the two opposite Rabi sidebands (R, L) for positive and reverse time orderings in the cases of positive and negative time delays. The two-photon emission channels $|k_A\rangle \xrightarrow{a_1} |k'_A\rangle \xrightarrow{a_2} |j_A\rangle$ or $|k_A\rangle \xrightarrow{a_2} |k'_A\rangle \xrightarrow{a_1} |j_A\rangle$ are indicated by the corresponding final-state two-photon probability amplitude $\mathcal{C}_j^{(k)}(\tau)$.

Two-photon channel	Positive (Reverse) time ordering for $\tau > 0 (\tau < 0)$	Reverse (Positive) time ordering for $\tau > 0 (\tau < 0)$	Time-ordering interference
$\lvert\mathcal{C}_1^{(1)}(\tau)\rvert^2$	$2 + 2\cos(\eta_1 + \eta_2)$	0	0
$\lvert\mathcal{C}_2^{(2)}(\tau)\rvert^2$	$(1 - \cos\eta_1)(1 - \cos\eta_2)$	$(1 - \cos\eta_1)(1 - \cos\eta_2)$	$2(1 - \cos\eta_1)(1 - \cos\eta_2)$
$\lvert\mathcal{C}_3^{(2)}(\tau)\rvert^2$	$(1 - \cos\eta_1)(1 + \cos\eta_2)$	$(1 + \cos\eta_1)(1 - \cos\eta_2)$	$-2\sin\eta_1 \sin\eta_2$
$\lvert\mathcal{C}_2^{(3)}(\tau)\rvert^2$	$(1 + \cos\eta_1)(1 - \cos\eta_2)$	$(1 - \cos\eta_1)(1 + \cos\eta_2)$	$-2\sin\eta_1 \sin\eta_2$
$\lvert\mathcal{C}_3^{(3)}(\tau)\rvert^2$	$(1 + \cos\eta_1)(1 + \cos\eta_2)$	$(1 + \cos\eta_1)(1 + \cos\eta_2)$	$2(1 + \cos\eta_1)(1 + \cos\eta_2)$
$\lvert\mathcal{C}_4^{(4)}(\tau)\rvert^2$	0	$2 + 2\cos(\eta_1 + \eta_2)$	0

pears completely. This distribution of time orderings indicates that it is entirely possible for positive time ordering to be prepared deterministically without the accompany of reverse time ordering, which may generate more strongly bunched two-color photon statistics. Figure 5(c) shows the significant asymmetry of temporal photon statistics prepared by the laser field with appropriately large detuning, under which the dressed two-atom system is predominantly trapped in the dressed state $|1_A\rangle$. In this case, the stronger temporal two-color bunching effect can be generated only for the specific detection order of positive time delay. Figure 5(d) further reveals the correlation components triggered by each dressed states. It can be seen that the positive time ordering triggered by the dressed state $|4_A\rangle$ [magenta circular line in Fig. 5(d)] for negative time delay is significantly suppressed, whereas the full two-photon statistics is predominantly contributed by the two-photon strongly correlated emissions triggered by the dressed state $|1_A\rangle$ [red dashed line in Fig. 5(d)]. In this circumstance, the constructive quantum interference between the positive time orderings of two two-photon cascaded emission channels $|1_A\rangle \xrightarrow{a_1} |2_A\rangle \xrightarrow{a_2} |1_A\rangle$ and $|1_A\rangle \xrightarrow{a_1} |3_A\rangle \xrightarrow{a_2} |1_A\rangle$ is established, as sketched in Fig. 3(b), and can be probed only under the detection order of positive time delay.

Now let us return to the conditions (24a) and (24b) again for some additional interesting properties. It should be pointed out that whether the directions at $\theta_2 = 0$ or $\theta_2 = \pi$ can maximize the new directional function $\Theta(\theta_1, \theta_2)$ depends on the first observation angle θ_1. Only in the range of $0 \leqslant \theta_1 \leqslant \pi/2$ does the direction $\theta_2 = 0$ correspond to the secondary maximum., whereas if $\pi/2 \leqslant \theta_1 \leqslant \pi$, the secondary maximum is switched to the opposite direction $\theta_2 = \pi$. This means that, for the secondary maximum of two-photon correlation for positive time delay, the same detection angle cannot be achieved and the angular combination (θ_1, θ_2) is always directionally asymmetric. This is different from the detection angles of principal maximum of two-photon correlation, which can be equal or distributed symmetrically. For $r_{12} = \lambda/2$, the angular combinations $(\theta_1, \theta_2) = (0, 0), (\pi, \pi)$, and $(\theta_1, \pi \pm \theta_1)$ for the principal maximum of two-photon correlation can be predicted by Eq. (24b), at which the two quantum sensors receive photons synchronously along the atomic axis, as sketched in Fig. 6(a), or are strictly symmetric with respect to the vertical line of the atomic axis, as sketched in Figs. 6(b) and 6(c) (blue solid arrows and green dashed arrows).

C. Space-time nonclassical correlations

We now further explore the space-time nonclassical properties of the two-atom strongly correlated Mollow photons generated by the above two schemes. The nonclassical correlation of radiation fields can be effectively tested by the Cauchy-Schwarz inequality in terms of the intensity-intensity correlations of radiation fields. In view of the fact that both the frequency-resolved version and multipoint space-time-dependent version of the Cauchy-Schwarz inequality have been proposed in Refs. [53–55], it is straightforward to generalize the intensity-intensity Cauchy-Schwarz inequality into the frequency-space-time-resolved version for our system in terms of the sensor modes, which takes the form of

$$\mathcal{R}_{12} = \frac{\left[G_{12}^{(2)}(\theta_1, 0; \theta_2, \tau)\right]^2}{G_1^{(2)}(\theta_1) G_2^{(2)}(\theta_2)} \leqslant 1, \tag{25}$$

where the single-point two-photon intensity-intensity correlation functions $G_l^{(2)}(\theta_l) (l \in \{1, 2\})$ can be obtained by setting the two quantum sensors to be synchronous, i.e., $\nu_1 = \nu_2$ and $\mathbf{R}_1 = \mathbf{R}_2$. The violation of the Cauchy-Schwarz inequality, i.e., $\mathcal{R}_{12} > 1$, indicates the nonclassical correlation of radiation fields in different space-time points. To investigate the influence of the intensity-intensity autocorrelations of the two-atom Mollow photons in Eq. (25) on the space-time nonclassical correlation properties, we plot their angular distributions for a large laser detuning in Fig. 7. By comparing with the single-photon radiation intensities in Fig. 4(a), it can be found that the angular distributions of intensity and intensity-intensity autocorrelation are qualitatively similar. For the central-band Mollow photon, both the intensity and intensity-intensity autocorrelation are maximal in the direction $\theta_2 = \pi/2$ and are suppressed in the directions $\theta_2 = 0$ and π for $r_{12} = \lambda/2$. However, the intensity-intensity autocorrelation of Rabi sideband photon still cannot display directionality. This suggests that the spatial-temporal behavior of the Cauchy-Schwarz inequality parameters should be coincident with that of the two-color two-photon statistics

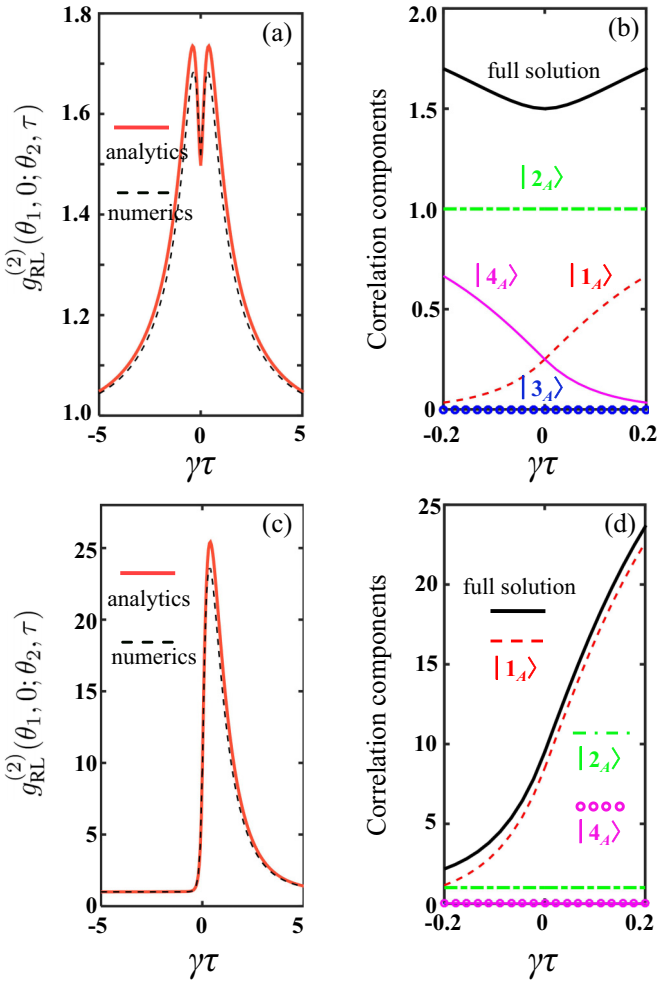

FIG. 5. Two-photon correlation $g^{(2)}_{\rm RL}(\theta_1,0;\theta_2,\tau)$ and the corresponding correlation components. (a), (b) Two-photon correlations for $\Delta_{\rm L}=0$ and $(\theta_1,\theta_2)=(0,\pi)$. (c), (d) Two-photon correlations for $\Delta_{\rm L}=-100\gamma$ and $(\theta_1,\theta_2)=(0,\pi)$. Other parameters are $\Omega=100\gamma$, $\kappa=10\gamma$, $\delta_1=0$, $\delta_2=0$, and $r_{12}=\lambda/2$. (a), (c) Comparison of the analytic solutions of arbitrary time delay (red solid lines) with broad filtering approximation and the numerical solutions of arbitrary time delay (black dashed lines) with the spontaneous decay rates of the atoms considered in Eq. (11b). (b), (d) Components of the full value of $g^{(2)}_{\rm RL}(\theta_1,0;\theta_2,\tau)$ (black solid lines) triggered by the dressed states $|1_A\rangle$ (red dashed lines), $|2_A\rangle$ (green dotted-dashed lines), and $|4_A\rangle$ (magenta circular line).

discussed in the above. In physical terms, the single-photon emission of central-band photon does not affect the single-atom dressed state. Thus the two-photon emission triggered by the initial dressed state $|1_A\rangle$, for example, is generated only from the single two-photon cascaded transition $|1_A\rangle\rightarrow|1_A\rangle\rightarrow|1_A\rangle$ without two-channel quantum interference, in which the spatial phase congruency of the cascaded single-photon transitions is maintained. Therefore, the directionality of two-photon state of the central-band photon is coincident with that of single-photon state. However, the sideband photon pairs are generated by the two-channel quantum interference $|1_A\rangle\rightarrow|2_A\rangle\rightarrow|4_A\rangle$ and $|1_A\rangle\rightarrow|3_A\rangle\rightarrow|4_A\rangle$, in which the destructive interference of internal-state

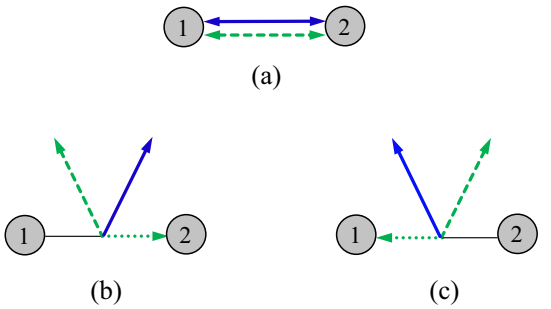

FIG. 6. Angular distribution and combination of $g^{(2)}_{\rm RL}(\theta_1,0;\theta_2,\tau)$ for $r_{12}=\lambda/2$ at which the pronounced asymmetry of temporal photon statistics and strong bunching effect only for positive time delay as shown in Fig. 5(c) can be achieved. The blue solid arrows represent the emission directions of the right-sideband photons. The green dashed and green dotted arrows represent the emission directions of the left-sideband photons, at which the principal maximum and secondary maximum can be probed, respectively. (a) The principal maximum is determined by $\cos\theta_1+\cos\theta_2=\pm2$, i.e., $\theta_1=\theta_2=0$ or π. (b), (c) The principal maximum is determined by $\cos\theta_1+\cos\theta_2=0$, i.e., $\theta_1=\pi\pm\theta_2$, while the secondary maximum is determined by $\theta_2=0$ (green dotted arrow) for $0\leqslant\theta_1\leqslant\pi/2$ (blue solid arrow) in (b) or $\theta_2=\pi$ (green dotted arrow) for $\pi/2\leqslant\theta_1\leqslant\pi$ (blue solid arrow) in (c).

transitions eliminates the relative spatial phase of the two-photon cascaded channels, with the consequence of the directionally uniform two-photon emission. We present the spatial-temporal distributions of the Cauchy-Schwarz inequality parameter $\mathcal{R}_{\rm RC}$ between the right Rabi sideband and the central band in Figs. 8(a) and 8(b) for different interatomic distances $r_{12}=\lambda/2$ and λ conditioned on the direction $\theta_1=0$, and the Cauchy-Schwarz inequality parameter $\mathcal{R}_{\rm RL}$ between the opposite Rabi sidebands in Figs. 8(c) and 8(d) for different directions $\theta_1=0$ and $\pi/4$. It can be seen clearly that the directions of giant violations of the Cauchy-Schwarz inequality are in accordance with the directions of bunching

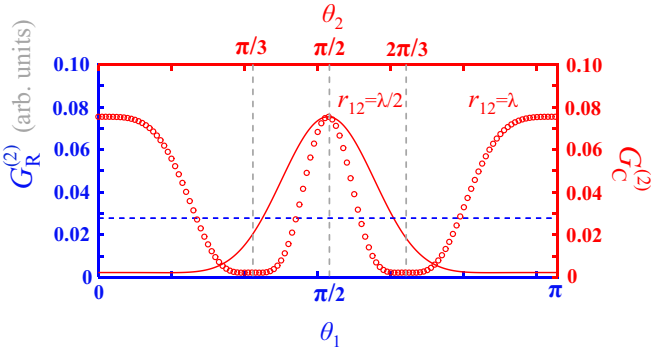

FIG. 7. Angular distribution of the frequency-resolved intensity-intensity autocorrelations $G^{(2)}_{\rm R}(\theta_1)$ and $G^{(2)}_{\rm C}(\theta_2)$ for the laser detuning $\Delta_{\rm L}=-100\gamma$. The blue dashed line correspond to $G^{(2)}_{\rm R}(\theta_1)$, and its direction-independent feature persists to the variation of the sub-wavelength interatomic distance $r_{12}(\sim\lambda)$. The red solid line and red circular line correspond to $G^{(2)}_{\rm C}(\theta_2)$ for $r_{12}=\lambda/2$ and λ, respectively. Other parameters are $\Omega=100\gamma$, $\kappa=10\gamma$, $\delta_1=0$, $\delta_2=0$, and $\theta_1=0$.

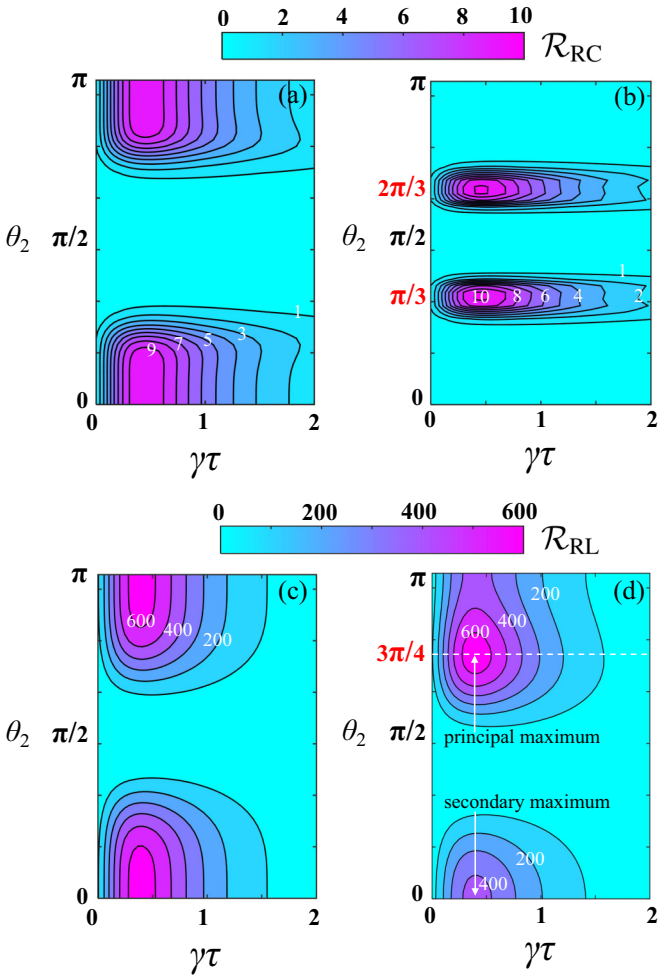

FIG. 8. Contour plot of the Cauchy-Schwarz inequality parameters $\mathcal{R}_{RC}$ and $\mathcal{R}_{RL}$ as functions of the time delay τ and the observation angle θ_2. (a), (b) $\mathcal{R}_{RC}$ for $\theta_1 = 0$ and (a) $r_{12} = \lambda/2$ and (b) $r_{12} = \lambda$. (c), (d) $\mathcal{R}_{RL}$ for $r_{12} = \lambda/2$ and (c) $\theta_1 = 0$ and (d) $\theta_1 = \pi/4$. Other parameters are $\Omega = 100\gamma$, $\Delta_L = -100\gamma$, $\kappa = 10\gamma$, $\delta_1 = 0$, and $\delta_2 = 0$.

effect predicted by the geometric conditions we discussed in the above. In particular, one can see from Fig. 8(d) that the violation of the Cauchy-Schwarz inequality displayed by the secondary maximum of $g^{(2)}_{RL}(\theta_1, 0; \theta_2, \tau)$ can be also pronounced in the direction $\theta_2 = 0$. It is worth noting that the violations of the Cauchy-Schwarz inequality of the Mollow resonance fluorescence have been noticed in the Dicke model [56] and the laser-dressed atomic ensemble [57] led by the two-photon resonance between two laser photons and Mollow photon pair.

IV. COMPARISONS

We would like to finish our discussion by comparing the present work with some previous work to show some connections and principal differences between the subwavelength laser-dressed two-atom system and the laser-dressed Dicke model [56,58] and the laser-dressed atomic ensemble [57].

A. Comparison with the Dicke model

In Refs. [56,58] the Mollow spectral correlations and nonclassicality were investigated in the Dicke model in which the equal-time anticorrelation between the sideband photons and central-band photons was discovered. However, in the present work, the bunching effect (strong correlation) of this two-color spectral combination is predicted in some directions. This indicates that the Mollow photon pairs of same two-color spectral combinations can exhibit qualitatively different photon statistical properties from different atomic geometric configurations. Let us take two-atom Dicke model as an example for our analysis. For the subwavelength dressed two-atom system, if we work in the collective dressed-state picture $|\tilde{1}(\tilde{4})_A\rangle = |\pm_1\rangle|\pm_2\rangle$ and $|\tilde{2}(\tilde{3})_A\rangle = |\pm_1\rangle|\mp_2\rangle$, and still consider the case that the sensor modes a_1 and a_2 are tuned to be on resonance with the right Rabi sideband and central band, respectively, the filtering Hamiltonian is given by

$$\begin{aligned}\tilde{H}_I =& \tilde{g}_1[e^{i\mathbf{k}\cdot\mathbf{r}_1}(\tilde{R}_{31} + \tilde{R}_{42}) + e^{i\mathbf{k}\cdot\mathbf{r}_2}(\tilde{R}_{21} + \tilde{R}_{43})]a_1^\dagger \\ &+ \tilde{g}_2[\chi_+(\tilde{R}_{11} - \tilde{R}_{44}) + \chi_-(\tilde{R}_{22} - \tilde{R}_{33})]a_2^\dagger \\ &+ \text{H.c.}, \end{aligned} \tag{26}$$

where $\tilde{R}_{\mu\mu'} = |\tilde{\mu}_A\rangle\langle\tilde{\mu}'_A|$ is the transition operator between the collective dressed states, and $\tilde{g}_1 = g_1 = -g\cos^2\phi$ and $\tilde{g}_2 = \sqrt{2}\sin\phi\cos\phi$ are the effective filtering coupling rates. The far-field spatial interference factors $\chi_\pm = (e^{i\mathbf{k}\cdot\mathbf{r}_1} \pm e^{i\mathbf{k}\cdot\mathbf{r}_2})/\sqrt{2}$ have been introduced in the above analytic formalism. However, the Dicke model refers to the collective atomic system in which all the atoms are confined to a small volume with the spatial scale much smaller than the radiation wavelength [35]. The filtering Hamiltonian (26) thus can be simplified to the form of two-atom Dicke model by assuming all the spatial phase factors to be equal and $e^{i\mathbf{k}\cdot\mathbf{r}_j} = e^{i\mathbf{k}\cdot\mathbf{r}_{12}} = 1$ [35], yielding the filtering Hamiltonian of the laser-dressed two-atom Dicke model

$$\begin{aligned}\tilde{H}_I^{(\text{Dicke})} =& \tilde{g}_1(\tilde{R}_{21} + \tilde{R}_{31} + \tilde{R}_{42} + \tilde{R}_{43})a_1^\dagger \\ &+ \sqrt{2}\tilde{g}_2(\tilde{R}_{11} - \tilde{R}_{44})a_2^\dagger + \text{H.c.} \end{aligned} \tag{27}$$

Comparing the Hamiltonians (26) and (27), one can see that the central-band dressed-state transitions $\tilde{R}_{22}$ and $\tilde{R}_{33}$ vanish in the two-atom Dicke model due to the completely destructive interference ($\chi_- = 0$). As depicted in Fig. 9(a), according to the Hamiltonian (27), there are four dressed-state transitions in the two-atom Dicke model that can generate right-sideband photons (blue arrows), but only two of them successively trigger the emissions of central-band photons (red solid arrows). This indicates that, conditioned on a central-band photon, the conditional probability of detecting a right-sideband photon is less than the independent probability of detecting a right-sideband photon, giving rise to the anticorrelation in Ref. [58]. However, for the subwavelength two-atom system, as described by the Hamiltonian (26) and depicted in Fig. 9(a), due to the presence of the spatial phase factors, two additional two-photon cascaded emission channels $|\tilde{1}_A\rangle \to |\tilde{2}_A\rangle \to |\tilde{2}_A\rangle$ and $|\tilde{1}_A\rangle \to |\tilde{3}_A\rangle \to |\tilde{3}_A\rangle$ are recovered (red dashed arrows), which can be prominent to be detected in some directions by preparing the particular dressed state $|\tilde{1}_A\rangle = |+_1\rangle|+_2\rangle$. This indicates that once this

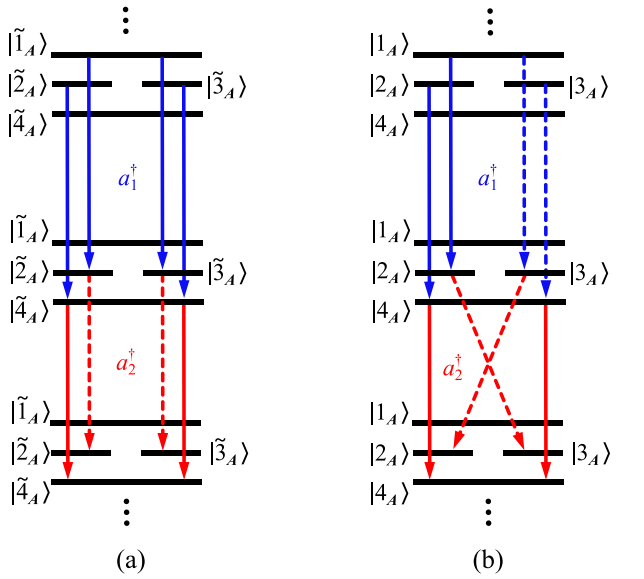

FIG. 9. Energy-level scheme of two-photon cascaded emissions in laser-dressed two-atom system (the two-atom Dicke model or the subwavelength two-atom system) in (a) two-atom collective dressed-state picture and (b) two-atom superposed dressed-state picture. The blue arrows and red arrows represent the dressed-state transitions generating the Mollow photons of the right (R) sideband and central (C) band, respectively, labeled by their respective sensor modes $a_1^\dagger$ and $a_2^\dagger$. The red dashed arrows represent the dressed-state transitions that cannot occur in the two-atom Dicke model due to completely destructive interference.

pair of privileged channels operates as positive time ordering, relatively large bunching can be probed. The same physical mechanism can also be gained if the energy-level diagram in Fig. 9(a) is transformed into the superposed dressed-state picture in Fig. 9(b) and can be generalized to the case of a large number of atoms in Ref. [58].

B. Comparison with the laser-dressed atomic ensemble

In Ref. [57] the theoretical work was devoted to the directional two-photon statistical properties and nonclassicality of the Mollow photons scattered from a strong laser-driven atomic ensemble, in which the strong correlations between different Mollow spectral lines of the propagation vectors $\mathbf{k}_1$ and $\mathbf{k}_2$ respectively are highly concentrated into the direction of propagation of the laser field, specified by the condition $\mathbf{k}_1 + \mathbf{k}_2 \approx 2\mathbf{k}_\mathrm{L}$. This single directionality is due to the configuration averaging procedure for interatomic distance vectors $\mathbf{r}_{ij}$ with the spatial interference that arises from the internal geometric structures of the collective radiating source being washed out. Thus the directionality is determined only by and with respect to the external laser field, leading to the more strongly correlated scattering of only the Mollow photon pairs that satisfy the two-photon resonance $\mathbf{k}_1 + \mathbf{k}_2 \approx 2\mathbf{k}_\mathrm{L}$. However, in contrast to the atomic ensemble, for the subwavelength two-atom system as well as other multiatom systems with regular geometric configurations, such as one-dimensional atomic chains [17,59], the spatial distribution of their radiative properties is not only determined by the incident direction of the laser field, but also determined exquisitely by the spatial coherence led by the internal geometric structures, i.e., the spatial phase factor $e^{i\mathbf{k}\cdot\mathbf{r}_j}$, which plays a key role in classical antenna theory [9]. In other words, the fineness of geometry and the resulting sensitivity of directionality of laser-driven atomic ensembles are between single-atom systems and subwavelength collective atomic systems. Compared with single-atom systems, laser-driven atomic ensembles have been provided with a certain ability to generate directionality, but it is not as rich as that generated by subwavelength collective atomic systems with regular geometry.

V. CONCLUSION AND PERSPECTIVES

We unveiled the space-time relationship between the time-domain two-color photon statistics and the spatial directionality of the frequency-resolved collective Mollow resonance fluorescence radiated from a laser-dressed two-atom system, and proposed the theoretical schemes of generating time-domain strongly correlated two-color Mollow photon pairs with high directionality and nonclassicality.

We constructed the spatial two-point photon filtering by applying a pair of quantum sensors, whose frequencies are tuned to be on resonance with different characteristic frequencies of the Mollow triplet. Under the condition of broad filtering bandwidth, we solved analytically the intensity-intensity two-time correlations of the filtered Mollow photons in terms of the sensor modes for different Mollow spectral combinations. The obtained analytic formalism enables us to analyze the directional properties of time orderings, which is the core concept that closely connects time and space. For the Mollow spectral combination between one of the Rabi sidebands and the central band, a pair of two-photon cascaded emission channels triggered by different dressed states with positive time ordering and reverse time ordering respectively can be identified in some specific two-point direction combinations in the form of incoherent superposition. Under detuned driving, the dressed two-atom system is enforced to emit only through the single two-photon cascaded emission channel of positive time ordering. As a consequence, strongly bunched two-color Mollow photon pairs can be detected in some specific two-point direction combinations only for a specific two-photon detection order. As for the Mollow spectral combination between the opposite Rabi sidebands, a pair of two-photon cascaded emission channels both with positive time orderings can be triggered by the dressed state in which the dressed two-atom system is predominantly trapped by detuned driving. Thus, the constructive quantum interference between positive time orderings can be witnessed. We elucidated the geometric conditions under which the strongly bunched two-color Mollow photon pairs of this spectral combination also can be detected only for a specific two-photon detection order. By examining the space-time-dependent Cauchy-Schwarz inequalities of the frequency-resolved version, we further verified that both the temporal bunching effects of these two Mollow spectral combinations generated by the proposed geometric schemes are nonclassical. In addition, we presented a brief comparison of the photon statistical properties and

directionality generated by the subwavelength laser-dressed two-atom system and the Dicke model and the laser-dressed atomic ensemble.

Further ideas of this work can be considered from the following aspects: One is that the laser-dressed two-atom system can be placed in the quantum optical platforms with modified electromagnetic reservoir. This may be conducive to further improve the degrees of superbunching and directional focusing by the Purcell effect. The second is that the dressed two-atom system in free space can be generalized to the multiatom systems with more complex geometric configurations, in which all the atoms can be driven by a strong laser field, or only atoms at specific positions can be selectively driven. This conception caters to the current hot research frontier of multiatom array-type antennas with subwavelength spacing. In addition, the multipoint space-time quantum characteristics can be considered, which may open a full landscape of the space-time quantum characteristics of Mollow multiphoton physics. This work has set a theoretical groundwork for this problem. We hope that this work could enable the laser-dressed two-atom antenna to be harnessed in the designs of nonclassical light sources and quantum radars, and in the research fields of atom-photon-based quantum precision measurement physics and Mollow spectroscopy.

ACKNOWLEDGMENTS

We are particularly indebted to the anonymous referees for their valuable comments that helped us to improve the quality of this paper. This work was supported by the National Natural Science Foundation of China (Grants No. 12204414, No. 12175199, and No. 12174139) and the Science Foundation of Zhejiang Sci-Tech University (Grant No. 21062344-Y).

[1] T. Kosako, Y. Kadoya, and H. F. Hofmann, Nat. Photonics **4**, 312 (2010).
[2] K. G. Lee, X. W. Chen, H. Eghlidi, P. Kukura, R. Lettow, A. Renn, V. Sandoghdar, and S. Götzinger, Nat. Photonics **5**, 166 (2011).
[3] T. Shegai, S. Chen, V. D. Miljković, G. Zengin, P. Johansson, and M. Käll, Nat. Commun. **2**, 481 (2011).
[4] A. G. Curto, G. Volpe, T. H. Taminiau, M. P. Kreuzer, R. Quidant, and N. F. van Hulst, Science **329**, 930 (2010).
[5] P. Bharadwaj, B. Deutsch, and L. Novotny, Adv. Opt. Photon. **1**, 438 (2009).
[6] J. Rui, D. Wei, A. Rubio-Abadal, S. Hollerith, J. Zeiher, D. M. Stamper-Kurn, C. Gross, and I. Bloch, Nature (London) **583**, 369 (2020).
[7] A. Asenjo-Garcia, H. J. Kimble, and D. E. Chang, Proc. Natl. Acad. Sci. USA **116**, 25503 (2019).
[8] P.-O. Guimond, A. Grankin, D. V. Vasilyev, B. Vermersch, and P. Zoller, Phys. Rev. Lett. **122**, 093601 (2019).
[9] G. Y. Slepyan, S. Vlasenko, and D. Mogilevtsev, Adv. Quantum Technol. **3**, 1900120 (2020).
[10] A. Mikhalychev, D. Mogilevtsev, G. Ya. Slepyan, I. Karuseichyk, G. Buchs, D. L. Boiko, and A. Boag, Phys. Rev. Appl. **9**, 024021 (2018).
[11] I. Liberal, I. Ederra, and R. W. Ziolkowski, Phys. Rev. A **97**, 053847 (2018).
[12] I. Liberal, I. Ederra, and R. W. Ziolkowski, Photonics **6**, 14 (2019).
[13] S. Oppel, T. Buttner, P. Kok, and J. von Zanthier, Phys. Rev. Lett. **109**, 233603 (2012).
[14] S. Oppel, R. Wiegner, G. S. Agarwal, and J. von Zanthier, Phys. Rev. Lett. **113**, 263606 (2014).
[15] A. Classen, F. Waldmann, S. Giebel, R. Schneider, D. Bhatti, T. Mehringer, and J. von Zanthier, Phys. Rev. Lett. **117**, 253601 (2016).
[16] D. Bhatti, R. Schneider, S. Oppel, and J. von Zanthier, Phys. Rev. Lett. **120**, 113603 (2018).
[17] Q.-ul-A. Gulfam and Z. Ficek, Phys. Rev. A **98**, 063824 (2018).
[18] C. Monroe, Nature (London) **416**, 238 (2002).
[19] C. Weitenberg, M. Endres, J. F. Sherson, M. Cheneau, P. Schaub, T. Fukuhara, I. Bloch, and S. Kuhr, Nature (London) **471**, 319 (2011).
[20] M. Endres, H. Bernien, A. Keesling, H. Levine, E. R. Anschuetz, A. Krajenbrink, C. Senko, V. Vuletic, M. Greiner, and M. D. Lukin, Science **354**, 1024 (2016).
[21] V. E. Lembessis, A. A. Rsheed, O. M. Aldossary, and Z. Ficek, Phys. Rev. A **88**, 053814 (2013).
[22] R. Alaee, A. Safari, V. Sandoghdar, and R. W. Boyd, Phys. Rev. Res. **2**, 043409 (2020).
[23] C. Skornia, J. von Zanthier, G. S. Agarwal, E. Werner, and H. Walther, Phys. Rev. A **64**, 063801 (2001).
[24] J. von Zanthier, T. Bastin, and G. S. Agarwal, Phys. Rev. A **74**, 061802(R) (2006).
[25] C. H. R. Ooi, B.-G. Kim, and H.-W. Lee, Phys. Rev. A **75**, 063801 (2007).
[26] C. H. R. Ooi, Phys. Rev. A **75**, 043817 (2007).
[27] S. Mährlein, L. Götzendörfer, K. Günthner, J. Evers, and J. von Zanthier, Phys. Rev. Res. **2**, 013278 (2020).
[28] A. Ulhaq, S. Weiler, S. M. Ulrich, R. Roßbach, M. Jetter, and P. Michler, Nat. Photonics **6**, 238 (2012).
[29] S. Bounouar, M. Strauß, A. Carmele, P. Schnauber, A. Thoma, M. Gschrey, J.-H. Schulze, A. Strittmatter, S. Rodt, A. Knorr, and S. Reitzenstein, Phys. Rev. Lett. **118**, 233601 (2017).
[30] J. Schleibner, S. Bounouar, M. Strauß, S. Reitzenstein, A. Knorr, and A. Carmele, Phys. Rev. A **99**, 023813 (2019).
[31] C. Sánchez Muñoz and F. Schlawin, Phys. Rev. Lett. **124**, 203601 (2020).
[32] J. C. López Carreño, C. Sánchez Muñoz, D. Sanvitto, E. del Valle, and F. P. Laussy, Phys. Rev. Lett. **115**, 196402 (2015).
[33] J. C. López Carreño and F. P. Laussy, Phys. Rev. A **94**, 063825 (2016).
[34] J. C. López Carreño, C. Sánchez Muñoz, E. del Valle, and F. P. Laussy, Phys. Rev. A **94**, 063826 (2016).
[35] Z. Ficek and S. Swain, *Quantum Interference and Coherence: Theory and Experiments* (Springer, Berlin, 2005).

[36] I. Dotsenko, W. Alt, M. Khudaverdyan, S. Kuhr, D. Meschede, Y. Miroshnychenko, D. Schrader, and A. Rauschenbeutel, Phys. Rev. Lett. **95**, 033002 (2005).
[37] Y. Miroshnychenko, W. Alt, I. Dotsenko, L. Förster, M. Khudaverdyan, D. Meschede, S. Reick, and A. Rauschenbeutel, Phys. Rev. Lett. **97**, 243003 (2006).
[38] L. Béguin, A. Vernier, R. Chicireanu, T. Lahaye, and A. Browaeys, Phys. Rev. Lett. **110**, 263201 (2013).
[39] A. Görlitz, M. Weidemüller, T. W. Hänsch, and A. Hemmerich, Phys. Rev. Lett. **78**, 2096 (1997).
[40] G. Raithel, G. Birkl, W. D. Phillips, and S. L. Rolston, Phys. Rev. Lett. **78**, 2928 (1997).
[41] C. Cohen-Tannoudji, J. Dupont-Roc, and G. Grynberg, *Atom-Photon Interactions: Basic Processes and Applications* (Wiley, New York, 1992).
[42] E. Darsheshdar, M. Hugbart, R. Bachelard, and C. J. Villas-Boas, Phys. Rev. A **103**, 053702 (2021).
[43] Z. Ficek and R. Tanás, *Quantum-Limit Spectroscopy* (Springer, New York, 2017), Chap. 3, pp. 85–86.
[44] E. Shahmoon and G. Kurizki, Phys. Rev. A **89**, 043419 (2014).
[45] E. del Valle, A. Gonzalez-Tudela, F. P. Laussy, C. Tejedor, and M. J. Hartmann, Phys. Rev. Lett. **109**, 183601 (2012).
[46] D. I. H. Holdaway, V. Notararigo, and A. Olaya-Castro, Phys. Rev. A **98**, 063828 (2018).
[47] G. Nienhuis, Phys. Rev. A **47**, 510 (1993).
[48] C. A. Schrama, G. Nienhuis, H. A. Dijkerman, C. Steijsiger, and H. G. M. Heideman, Phys. Rev. A **45**, 8045 (1992).
[49] G. Nienhuis, Europhys. Lett. **21**, 285 (1993).
[50] K. Joosten and G. Nienhuis, J. Opt. B: Quantum Semiclass. Opt. **2**, 158 (2000).
[51] V. N. Shatokhin and S. Y. Kilin, Phys. Rev. A **94**, 033835 (2016).
[52] P. A. Apanasevich and S. Ja. Kilin, J. Phys. B: Atom. Mol. Phys. **12**, L83 (1979).
[53] A. González-Tudela, E. del Valle, and F. P. Laussy, Phys. Rev. A **91**, 043807 (2015).
[54] C. Sánchez Muñoz, E. del Valle, C. Tejedor, and F. P. Laussy, Phys. Rev. A **90**, 052111 (2014).
[55] W. Vogel, Phys. Rev. Lett. **100**, 013605 (2008).
[56] N. N. Bogolubov, Jr., A. S. Shumovsky, T. Quang, Phys. Lett. A **123**, 71 (1987).
[57] L. Jin, J. Evers, and M. Macovei, Phys. Rev. A **84**, 043812 (2011).
[58] N. N. Bogolubov Jr., E. I. Aliskenderov, A. S. Shumovsky, and T. Quang, J. Phys. B: Atom. Mol. Phys. **20**, 1885 (1987).
[59] Q.-ul-A. Gulfam and Z. Ficek, Phys. Rev. A **94**, 053831 (2016).